

Article

Spatial-Temporal Evolution and Cooling Effect of Irrigated Cropland in Inner Mongolia Region

Long Li ^{1,2}, Shudong Wang ¹, Yuwei Bo ³, Banghui Yang ⁴, Xueke Li ⁵ and Kai Liu ^{1,*}

¹ The State Key Laboratory of Remote Sensing Science, Aerospace Information Research Institute, Chinese Academy of Sciences, Beijing 100094, China; lilong221@mails.ucas.ac.cn (L.L.); wangsd@aircas.ac.cn (S.W.)

² University of Chinese Academy of Sciences, Beijing 101408, China

³ Shandong Provincial NO. 4 Institute of Geological and Mineral Survey, Weifang 261021, China

⁴ Aerospace Information Research Institute, Chinese Academy of Sciences, Beijing 100094, China; yangbh@aircas.ac.cn

⁵ The Department of Earth and Environmental Science, University of Pennsylvania, Philadelphia, PA 19104, USA; xuekeli@sas.upenn.deu

* Correspondence: liuk@aircas.ac.cn

Abstract: Monitoring the dynamic distribution of irrigated cropland and assessing its cooling effects are essential for advancing sustainable agriculture amid climate change. This study presents an integrated framework for irrigated cropland monitoring and cooling effect assessment. Leveraging dense time series vegetation indices with Google Earth Engine (GEE), we evaluated multiple machine learning algorithms within to identify the most robust approach (random forest algorithm) for mapping irrigated cropland in Inner Mongolia from 2010 to 2020. Furthermore, we developed an effective method to quantify the diurnal, seasonal, and interannual cooling effects of irrigation. Our generated irrigated cropland maps demonstrate high accuracy, with overall accuracy ranging from 0.85 to 0.89. This framework effectively captures regional cropland expansion patterns, revealing a substantial increase in irrigated cropland across Inner Mongolia by 27,466.09 km² (about +64%) between 2010 and 2020, with particularly pronounced growth occurring after 2014. Analysis reveals that irrigated cropland lowered average daily land surface temperature (LST) by 0.25 °C compared to rain-fed cropland, with the strongest cooling effect observed between July and August by approximately 0.64 °C, closely associated with increased evapotranspiration. Our work highlights the potential of satellite-based irrigation monitoring and climate impact analysis, offering a valuable tool for supporting climate-resilient agriculture practices.

Keywords: irrigated cropland; land use change; cooling effect; remote sensing; Google Earth Engine; machine learning



Citation: Li, L.; Wang, S.; Bo, Y.; Yang, B.; Li, X.; Liu, K. Spatial-Temporal Evolution and Cooling Effect of Irrigated Cropland in Inner Mongolia Region. *Remote Sens.* **2024**, *16*, 4797. <https://doi.org/10.3390/rs16244797>

Academic Editor: Jochem Verrelst

Received: 29 October 2024

Revised: 11 December 2024

Accepted: 19 December 2024

Published: 23 December 2024



Copyright: © 2024 by the authors. Licensee MDPI, Basel, Switzerland. This article is an open access article distributed under the terms and conditions of the Creative Commons Attribution (CC BY) license (<https://creativecommons.org/licenses/by/4.0/>).

1. Introduction

Irrigated cropland refers to arable land with irrigation equipment, such as artificial ditches or pipelines, which use groundwater or surface water to ensure normal crop growth. This practice consumes large amounts of freshwater resources to achieve stable and increased yields. While irrigated agriculture accounts for about 20% of the world's cropland, it produces about 40% of the world's food and consumes about 70% of freshwater resources [1]. Irrigated cropland plays an important role in ensuring food security [2–4] and has been shown to have a large potential to mitigate regional climate warming [5,6]. Over the past decade, northern China has actively promoted water-saving irrigation projects, leading to a substantial expansion of irrigated cropland [7]. However, changes in the spatial distribution of irrigated cropland and its feedback on regional climate remain poorly understood [8,9].

Several studies have been conducted to either map irrigated cropland [10–12] or assess the cooling effects of irrigation [13–15]. However, these two areas of research are often

treated separately, with many studies focusing exclusively on one or the other. This results in existing maps of irrigated cropland often being inadequate for accurately assessing the regional cooling effects of irrigation. The challenges include the following: (a) many existing maps focus solely on irrigated areas, neglecting non-irrigated cropland [14]; (b) global or national-scale irrigated cropland maps lack the resolution needed for accurate regional analysis [16]; and (c) studies often use land surface temperatures (LST) as a feature for mapping irrigated cropland [17,18], which may bias the assessment of cooling effects. To overcome these challenges, a research framework is needed to assess both the spatial dynamics of irrigated cropland and the associated climate impacts.

Accurate mapping of irrigated cropland is a crucial prerequisite for evaluating its cooling effects. Irrigated cropland mapping is typically approached from three perspectives: (a) the use of national and regional statistics [11,19], (b) irrigation performance [12,16], and (c) the biophysical effects of irrigation [20–22]. The spatial allocation method is the primary approach for mapping irrigated cropland using statistical data [23]. This method enables the creation of global or national-scale maps by integrating expert knowledge of irrigation suitability or vegetation indices reflecting crop growth, although collecting and updating statistical data is challenging, and variations in statistical standards and quality exist [16]. Nevertheless, these maps are widely recognized due to their high consistency with the statistical data [24,25]. Regional agriculture and water resource management require more-detailed maps of irrigated cropland. The resolution of maps based on statistical data is too coarse to meet these demands [16]. To address this, several methods have been proposed to generate finer maps, focusing on irrigation performance and biophysical effects of irrigation [12,20]. Irrigated crops enhanced growth due to irrigation, which is reflected in vegetation indices such as NDVI, EVI, and GI [18,26]. Biophysical effects include changes in surface temperature, soil moisture and evapotranspiration caused by irrigation. Threshold-based methods have been used to differentiate irrigated from non-irrigated areas based on crop growth [12,27]. Alternatively, maps can be derived by detecting irrigation-induced soil moisture anomalies [20,21]. However, using surface temperature parameters during mapping may bias the assessment of cooling effects. Therefore, methods focusing on crop growth are needed to ensure high accuracy and reliability. Machine learning, with its ability to handle high-dimensional time-series data, is particularly promising for this task [18,28,29].

Irrigation is a classic example of anthropogenic influence on near-surface climate. Numerous studies have shown that irrigation has a cooling effect, benefiting crop yields and human health [30–32]. While land surface models and algorithms have been used to assess the cooling effect of irrigation [33,34], challenges remain in achieving precise regional assessments. Land surface models tend to produce coarse results [35] suitable for the national or global scale but inadequate for regional applications. For instance, Yang designed the Irrigation Cooling Effect Detection (ICED) method [14], which uses satellite observations to assess the cooling effect of irrigated cropland in China. The application of the ICED algorithm in regions with low levels of non-irrigated cropland presents some challenges. The algorithm uses a neighborhood search to evaluate the difference in LST between irrigated and non-irrigated cropland. However, in arid climates where non-irrigated cropland is scarce, grasslands are often used as substitutes, which introduces uncertainty into the results [14]. Therefore, the method needs to be redesigned to better detect the cooling effect of irrigation in arid climate zones.

To address these gaps, this study proposes an integrated framework that combines high-frequency time-series data with machine learning techniques. Our framework leverages dense vegetation time-series indices to capture irrigated cropland growth and phenological differences while incorporating topographic parameters to enhance mapping accuracy. Multiple machine learning algorithms were evaluated within the Google Earth Engine platform to identify the most effective model for mapping irrigated cropland dynamics across Inner Mongolia from 2010 to 2020. Based on these detailed irrigated cropland maps, we further employed a moving window strategy to quantify the irrigation cooling

effect, followed by an analysis of the factors influencing this cooling impact. Our study is expected to enhance the accuracy of regional irrigation monitoring, providing insights into how irrigation contributes to local climate regulation, particularly in semi-arid and arid regions vulnerable to climate stress.

2. Materials and Methods

2.1. Study Area

The study area is Inner Mongolia, China ($97^{\circ}12'–126^{\circ}04'E$, $37^{\circ}24'–53^{\circ}23'N$), located in a mid-latitude arid and semi-arid region with a predominantly temperate continental climate (Figure 1), with precipitation in the range of 150–450 mm and uneven spatial and temporal distribution in most areas [36]. The large east–west span of the study area and pronounced east–west hydrothermal gradients provide a diverse range of climatic conditions, making it an ideal setting to validate the robustness of the irrigated cropland mapping methodology and assess the irrigation cooling effect across varying climates [37].

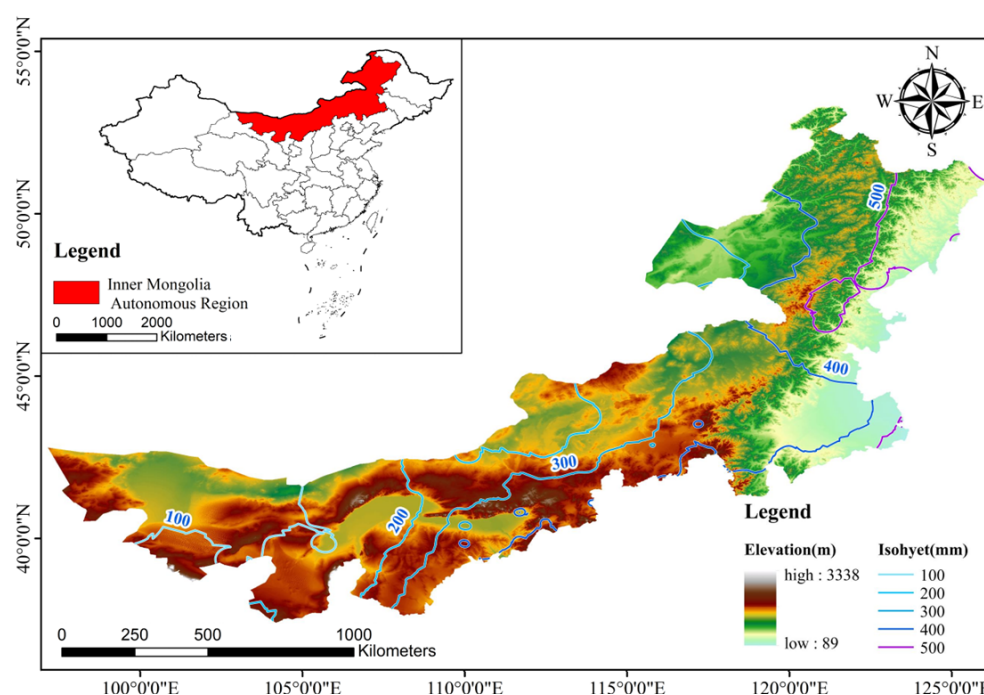


Figure 1. Map of geographical location of Inner Mongolia.

2.2. Datasets and Data Processing

The main data used in this study include the MODIS vegetation index dataset, the MODIS LST dataset, the MODIS evapotranspiration dataset, and topographic data. In addition, we used medium- to high-resolution Landsat data and Sentinel-2 data to assist in labeling the samples (Table 1). All data used in the study are available in the Google Earth Engine (GEE) dataset archive (<https://developers.google.com/earth-engine/datasets/>, accessed on 29 November 2024) and can be preprocessed and downloaded in GEE.

The vegetation index dataset used in this study was the MOD13Q1 product. The MOD13Q1 product is derived from the Moderate Resolution Imaging Spectrometer on Terra and is generated at a spatial resolution of 250 m every 16 days. The MOD13Q1 product provides two main layers of Normalized Vegetation Index (NDVI) and Enhanced Vegetation Index (EVI), and the MOD13Q1 product's synthesis algorithm selects the best available pixel values from all acquisitions over the 16-day period, using low cloud, low view, and highest NDVI/EVI values [38]. Since NDVI has good characterization of vegetation growth conditions [39], resulting in differences in NDVI time profiles between irrigated and rain-fed cropland [40], it is widely used in mapping studies of irrigated cropland [41,42]. However, NDVI uses nonlinear stretching to enhance the contrast between near-infrared and red

band reflectance, which makes NDVI have lower sensitivity for high-vegetation areas [43], while crops generally have higher NDVI, and it may be difficult to achieve satisfactory mapping accuracy using only NDVI. EVI, which has higher sensitivity in high-biomass areas, has addressed the saturation effect of NDVI [44].

Table 1. Summary of datasets used in this study.

Data Sources	Bands	Spatial Resolution	Temporal Resolution	Purpose
MOD13Q1	NDVI, EVI	250 m	16 d	Classification
MOD11A2	LST_Day_1km, LST_Night_1km	1000 m	8 d	Cooling effect analysis
MOD16A2	ET	500 m	8 d	Cooling effect analysis
SRTM	Elevation	90 m	/	Classification
Landsat 5/7/8	NIR, Red, Green	30 m	16 d	Sample labeling
Sentinel-2	NIR, Red, Green	10 m	5 d	Sample labeling

Mapping of irrigated cropland using NDVI and EVI was preceded by quality control and data smoothing of the NDVI and EVI time series to minimize the impact of outliers. Time-series data smoothing was performed using Savitzky–Golay (S-G) filtering [45,46], which is commonly applied for smoothing MODIS data. Data smoothing mitigated the effects of outliers, while also preserving differences in phenology across land cover as much as possible (Figure 2).

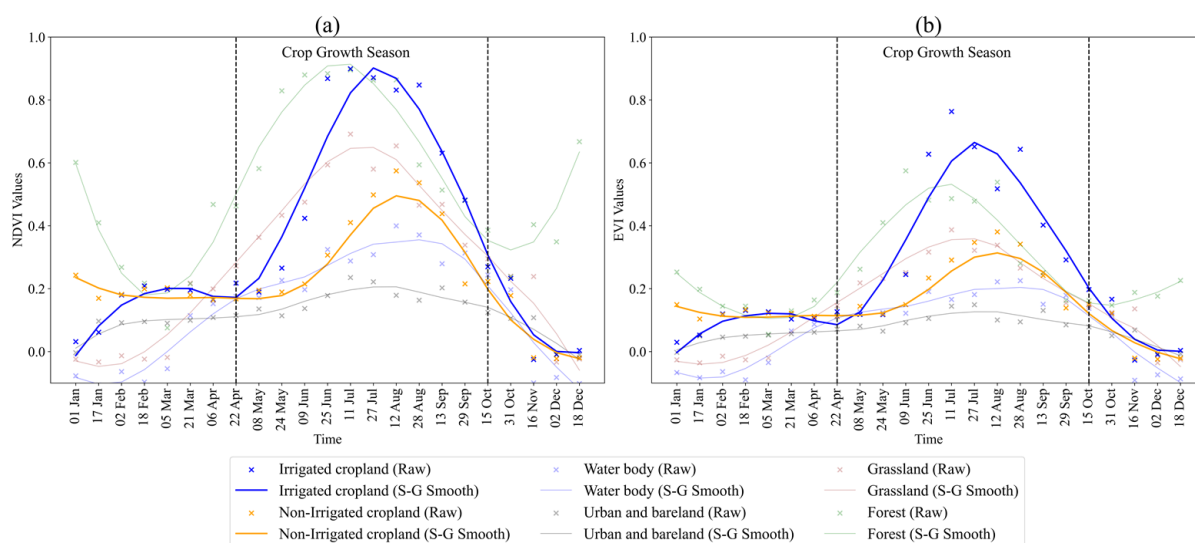


Figure 2. NDVI (a) and EVI (b) time-series smoothing results for different land cover.

The MOD11A2 product provides average LST for every 8 days at 1 km spatial resolution [47], and we used the daytime LST and nighttime LST layers from the data and calculated the daily mean LST and daily temperature range (DTR) from these two layers [48]. We examined the effect of irrigated cropland on daytime LST and nighttime LST and the effect of average daily LST and DTR calculated from the two layers separately by moving windows to measure the LST change due to irrigation. The MOD11A2 product underwent quality control to remove outliers and was synthesized into a monthly average LST.

The MOD16A2 product is based on the Penman–Monteith equation and estimates total evapotranspiration every 8 days by inputting daily meteorological reanalysis data and MODIS remotely sensed data products (e.g., dynamics of vegetation characteristics, albedo, and land cover) [49]. The MOD16A2 product was used to analyze the relation-

ship between irrigation cooling effects and surface evapotranspiration. The MOD16A2 product underwent quality control to remove outliers and was synthesized into a monthly average ET.

Shuttle Radar Topography Mission (SRTM) is an international research effort that obtained digital elevation models on a near-global scale [50]. We used the SRTM V3 product (SRTM Plus) from GEE provided by NASA JPL with a spatial resolution of about 90 m. This dataset was filled with blank areas using open source data (ASTER GDEM2, GMTED2010, and NED). During the sample collection, we found that some rain-fed croplands in Inner Mongolia are usually located in sloping areas, while irrigated croplands are located in relatively flat areas. Therefore, we calculated the slope from the 90 m DEM data and downsampled to 250 m to match the NDVI and EVI data.

2.3. Methods

This study consists of two main components, as illustrated in Figure 3. The first component focuses on classifying irrigated cropland in Inner Mongolia, using 2020 as a representative year. Critical steps in this part include the collection of classification samples, pre-processing of classification data, comparison of classifier accuracy, and validation of the final classification results. After verifying the accuracy and reliability of the classification method, we applied it to map the annual distribution of irrigated cropland in Inner Mongolia at a resolution of 250 m from 2010 to 2020. The second component quantifies the cooling effect of irrigated cropland. Indicators such as daytime LST, nighttime LST, average daily LST, and DTR were used to assess surface temperature differences between irrigated and rain-fed cropland. Employing a moving window strategy, we analyzed these indicators to capture spatial and temporal variations in the cooling effect and further explored the relationship between irrigation-driven crop transpiration and LST.

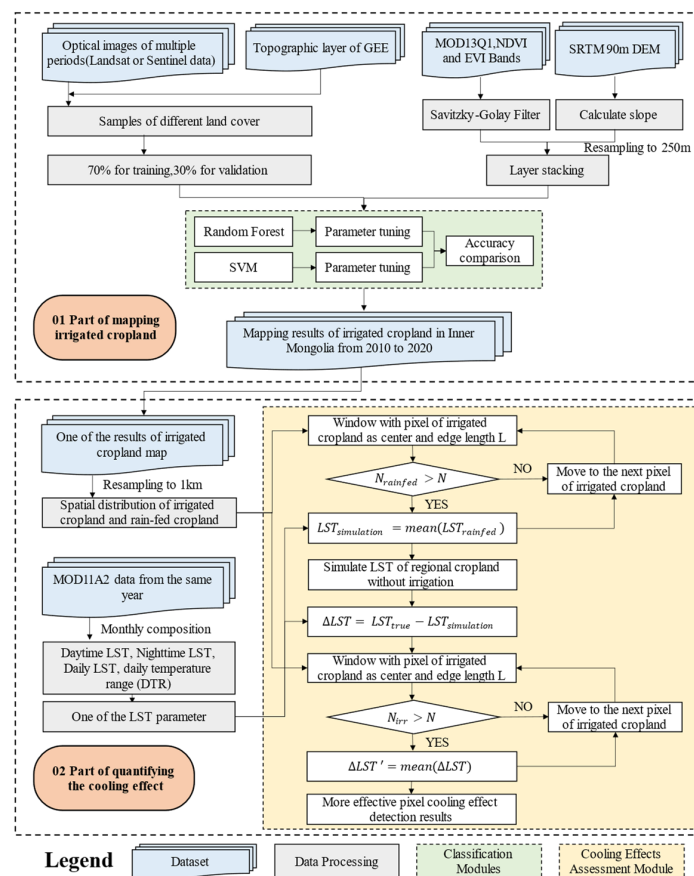


Figure 3. Flowchart of the study. The flow of the study was divided into two parts: part 1 focused on mapping irrigated cropland, and part 2 focused on assessing the cooling effects.

2.3.1. Classification System and Sample Collection

This study focuses on distinguishing between irrigated and rain-fed cropland to analyze the cooling effect of irrigation on LST, hence a robust classification system was essential for accurate analysis. In this study, cropland was categorized into irrigated cropland and rain-fed cropland. Considering the presence of a large number of fallow, abandoned, and retired croplands in the study area, an existing cropland mask was not used to remove the non-cropland areas. Instead, according to the actual situation of the study area, five types of ground cover, namely forest, grassland, water, urban, and bare land, were included to remove the non-cropland areas. Urban and bare land were combined as a single category representing low vegetation cover, as these were not the focus of this study.

Sample collection is a critical part of supervised classification work, as the quality of samples directly affects classification accuracy. However, collecting multi-year samples is often time-consuming and labor-intensive. Leveraging the power of GEE, we were able to simultaneously display multi-year NDVI/EVI time-series curves for sample points during the same time as sample collection. Forestland, grassland, water bodies, towns and bare land were generated by randomly selecting points within the study area. Their land cover types were identified using multi-year NDVI/EVI time-series curves and 2020 true-color imagery, ensuring that selected points represented stable land cover types from 2010 to 2020.

Collection of irrigated and rain-fed cropland samples was still performed separately in different years to ensure the quality of the samples. The collection of samples of irrigated and rain-fed cropland was based on Google High-Definition (HD) imagery, with multi-temporal optical imagery as an auxiliary reference, mainly during the sowing period (early May), the growing period (July), and the ripening period (early September) (Figure 4a,c). The distance of the field from the water source and the irrigation conditions of the field were also taken into account. In addition, we travelled to the study area to make a field visit to assess the irrigation situation and to record the coordinates of irrigated and non-irrigated cropland (Figure 4b,d).

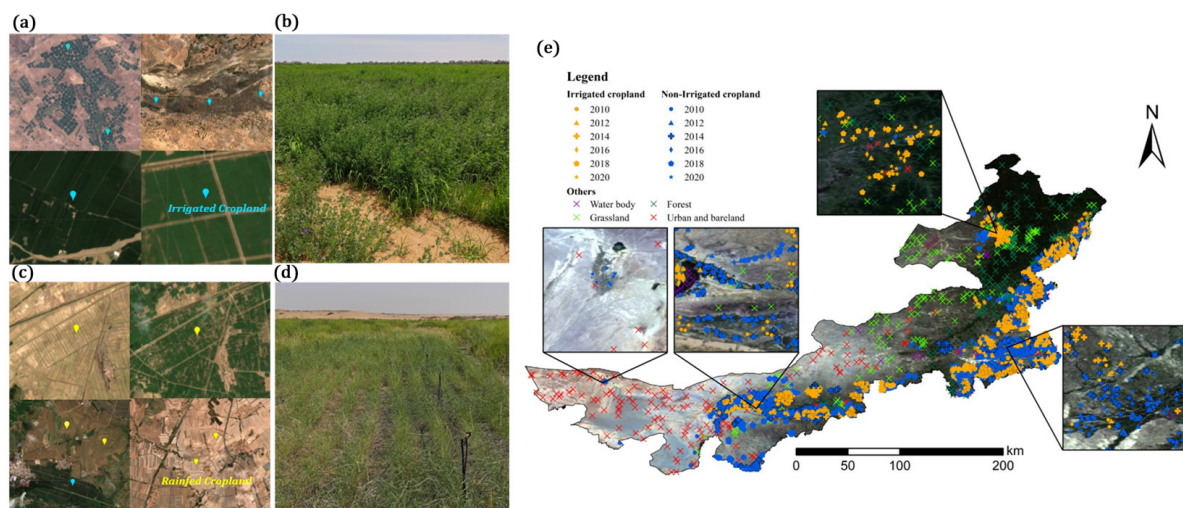


Figure 4. Irrigated cropland and rain-fed cropland on Google HD imagery and field photos. (a) and (c) are examples of irrigated and rain-fed cropland samples collected using Google HD imagery, respectively; (b,d) are field photographs of irrigated and rain-fed cropland, respectively, taken in July. (e) Spatial distribution of all samples collected.

The principles for discriminating irrigated cropland are [11,16] as follows: (1) cropland with visible irrigation facilities and in good tillage condition; (2) soil color is brownish in the absence of vegetation cover during the early stages of crop growth, showing a clear signal of high soil moisture; (3) crops are dark or light green during growth, with a uniform and subtle coloration (Figure 4a).

In contrast, rain-fed cropland was judged on the basis of (1) being far from water sources, with steep slopes and no significant irrigation; (2) uneven color and rough texture during the crop growth period; and (3) bright soil color at the beginning of the crop growth period, which exhibits a low soil moisture signal (Figure 4c).

All the samples were divided into training and validation samples in a 7:3 ratio. We collected samples from 2010 to 2020 (Figure 4e), with the total number of all land cover type samples as shown in Table 2.

Table 2. Number of samples for each land cover type, from 2010 to 2020.

Land Cover	2010	2012	2014	2016	2018	2020
Forest				211		
Grassland				180		
Water body				90		
Urban and bare land				215		
Irrigated cropland	503	421	447	426	494	575
Rain-fed cropland	360	326	366	305	369	478

2.3.2. Classification Methods

To accurately separate irrigated cropland, rain-fed cropland, and non-cropland, time-series NDVI and EVI were used as key classification features. Number studies have demonstrated the effectiveness of NDVI and EVI in mapping irrigated cropland [12,51,52]. In addition, slope, an important evaluation parameter of irrigation suitability, was incorporated as a classification feature. The Jeffries–Matusita distance (J–M distance) [53] analysis showed that the combination of slope, NDVI, and EVI features provided the best performance for separating different land classes (Figure A2). Therefore, 46 bands of NDVI and EVI data, with a 16-day step size per year, along with one slope factor, were selected as classification features.

With the development of machine learning techniques and the demand for classification accuracy, random forests and support vector machines are widely used in land cover classification studies [54–59]. In this study, the main parameters of RF and SVM were fine-tuned using the grid search method, optimizing overall accuracy as the evaluation metric. The powerful computational capabilities of Google Earth Engine (GEE) facilitated efficient tuning and ensured robust classification performance.

Random forest (RF) is an algorithm developed by Breiman, generally used in classification and regression studies, that operates by constructing a large number of decision trees at training time. Each tree grows independently to its maximum size based on bootstrap samples from the training dataset without any pruning, and each node is split using the best value from a subset of the input variables. Finally, random forest outputs the class chosen by most trees [60]. The parameters we need to set in random forest in GEE are numberOfTrees and variablesPerSplit [61]. Number of Trees in many studies is generally 100 to 2000, while variablesPerSplit defaults to the square root of the number of features [56], but Breiman argues that variablesPerSplit can be chosen between 1/2 and 2 times the square root of the number of features [60,62]. We input features of the random forest including 23 NDVI bands, 23 EVI bands, and 1 slope band, so we set numberOfTrees to range from 100 to 2000 in steps of 50 and variablesPerSplit to range from 3 to 14 in steps of 1.

Support vector machines (SVM) were developed by Vapnik et al. [63]. They can find hyperplanes between different classes of data with a small number of training samples, and then project these data from the input space to another higher dimensional feature space so that a linearly differentiable output dataset can be obtained. This projection process relies on a suitable kernel function, and there are four kernel functions in the SVM: LINEAR, POLY, RBF, and SIGMOID kernels. For land use classification, RBF is the most popular technique and has better accuracy than the other kernel functions [56,64]. The main parameters to be set for RBF in GEE are cost and gamma [65]; in this study cost is 10 m, $m = [-4, 4]$, and gamma is 10 n, $n = [-3, 3]$.

2.3.3. Methods for Quantifying the Cooling Effect of Irrigated Cropland

We employed a moving window-based method for detecting the cooling effect [14]. This method assumes a consistent climatic background within a certain range of windows and quantifies the cooling effect of irrigated cropland by comparing the LST of irrigated cropland with that of rain-fed cropland. Unlike approaches that adjust window size to increase the number of effective image elements, our method achieves this by reapplying the moving window. The exact procedure is as follows.

(a) Perform data preprocessing

We used classification data of irrigated and rain-fed cropland from the previous section and the daytime LST and nighttime LST data from MOD11A2. We resampled the classification data to 1 km to match the spatial resolution of the LST data. A grid was classified as irrigated cropland if irrigated cropland covered more than 80% of the 1 km area, and the same criterion was applied to rain-fed cropland. We calculated the daily average LST and DTR from the daytime and nighttime LST, then synthesized and downloaded the monthly LST data using GEE.

(b) Use moving windows to quantify cooling effects

For a given year, we combined the spatial distribution data of irrigated and rain-fed cropland with corresponding LST parameters. The average LST for all rain-fed cropland pixels within a window of side length L was calculated and used to replace the LST of the irrigated cropland pixel at the center of the window (Figure 5). To minimize anomalies caused by an insufficient number of rain-fed plowed pixels, calculations were performed only when the proportion of rain-fed pixels in the window exceeded a threshold N . The initial LST of irrigated cropland ($LST_{\text{irrigated}}$) was treated as the true value, while the result obtained by moving the window was regarded as the simulated value (LST_{rainfed}). The cooling effect of irrigated cropland was then obtained by the formula:

$$\Delta LST = LST_{\text{irrigated}} - LST_{\text{rainfed}}$$

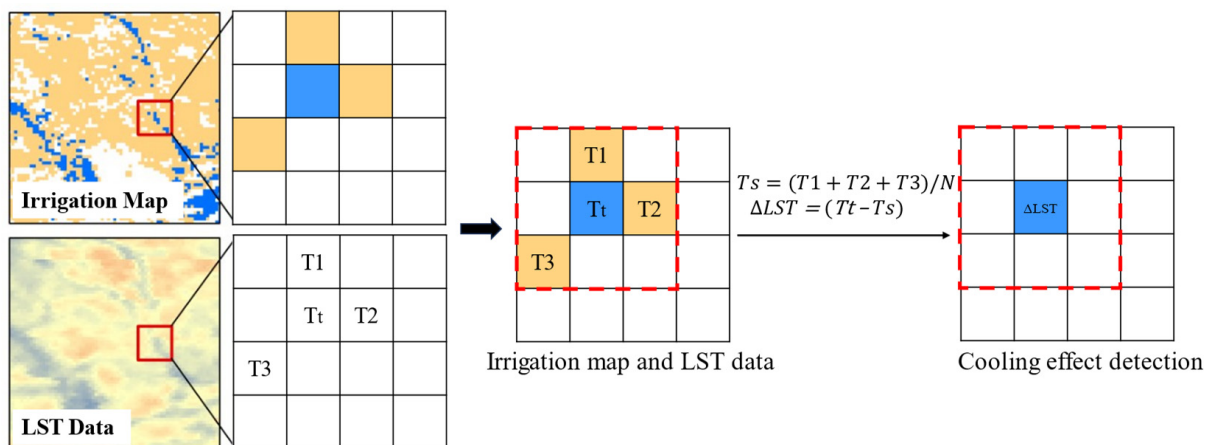


Figure 5. Schematic diagram for quantifying cooling effects using a moving window. Yellow patches indicate rain-fed cropland pixels, and blue patches indicate irrigated cropland pixels; T_1 to T_3 indicate LST for rain-fed cropland; T_t indicates LST for satellite observations of irrigated cropland; T_s indicates LST for pixels of irrigated cropland under simulated non-irrigated conditions; and ΔLST indicates the result of quantification of the cooling effect.

A positive ΔLST ($\Delta LST > 0$) indicates that irrigation increases the LST of cropland, while a negative ΔLST ($\Delta LST < 0$) indicates that irrigation decreases the LST of cropland.

(c) Re-apply the moving window to fill in the gaps

Due to the scarcity of rain-fed cropland in the study region, many irrigated cropland areas lacked nearby rain-fed cropland as a reference. Consequently, a significant number

of irrigated cropland pixels did not receive Δ LST after the initial execution of the moving window, potentially underestimating the regional irrigation cooling effect. To address this issue, we iteratively applied the moving window multiple times, based on the assumption that neighboring irrigated croplands have similar cooling effects. Specifically, for a given irrigated cropland pixel missing a cooling effect value, the gap was filled using the mean Δ LST of surrounding pixels within a moving window centered on the target pixel, using the same side length L.

The detection of the irrigated cropland cooling effect depends on two key parameters: the window size L and the proportion of rain-fed cropland pixels within the window. In this study, L was set to 21 km, and N was set to 10%, ensuring a balance between capturing sufficient rain-fed cropland reference pixels and maintaining reliable detection results.

3. Results

3.1. Optimal Parameter Combination of RF and SVM

We evaluated the classification performance of RF and SVM with different parameter combinations in terms of overall accuracy (OA) metrics to ensure the best classification results. The difference in OA obtained for different parameter combinations of RF was small. As shown in Figure 6, the highest OA (0.874) was achieved when number Of Tree = 1000 and variablesPerSplit = 10. In contrast, the OA for SVM varied considerably with different parameter combinations, with the highest OA (0.864) obtained when Gamma = 1 and Cost = 10. The comparison of the two machine learning algorithms indicated that RF produced more stable results, while SVM showed fluctuations in performance across the configuration. Furthermore, RF with optimized parameters outperformed SVM in terms of OA, making it the preferred algorithm for this study.

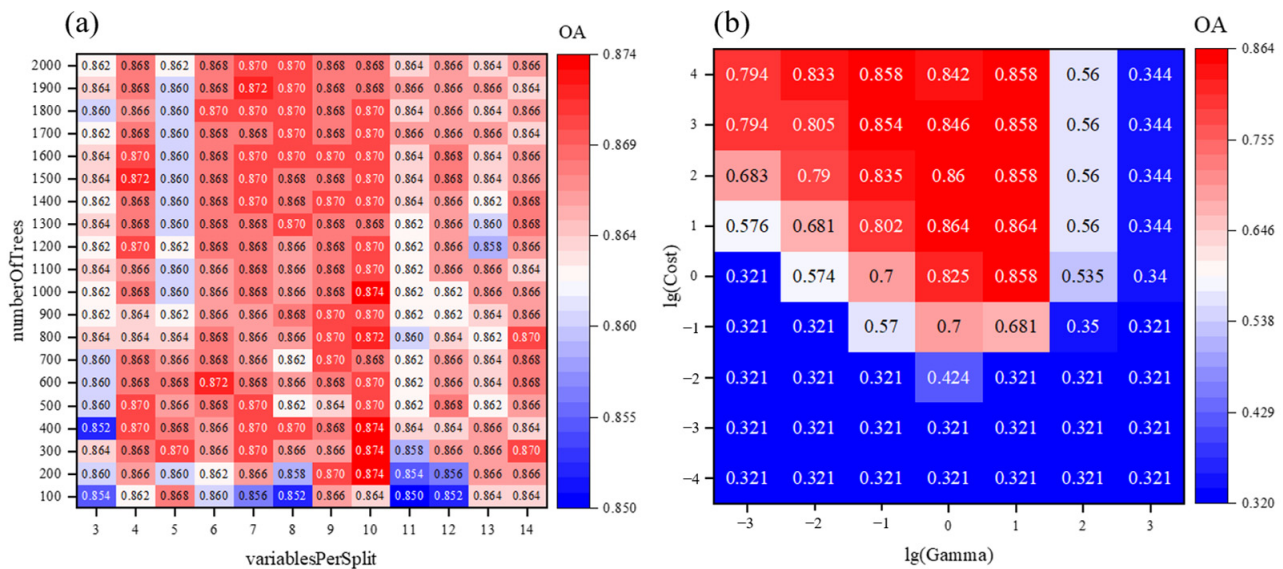


Figure 6. Grid search results for (a) RF classifiers and (b) SVM classifiers.

In fact, the large gap between Random Forest and SVM in the classification of irrigated cropland can be attributed to the high dimensionality of the input features. Random Forest generates classification results by aggregating votes from multiple decision trees, enabling it to handle high-dimensional and non-linear data more effectively [66]. This advantage has been widely demonstrated in land cover classification studies [67,68]. Given this, we selected RF to map the spatial distribution of irrigated cropland in Inner Mongolia. For each year, we optimized RF parameters using the same approach, ensuring the most accurate and reliable classification results.

3.2. Validation of Irrigated Cropland Maps

Accuracy validation was performed using a confusion matrix from independent validation samples. Overall accuracy (OA), user's accuracy (UA), producer's accuracy (PA), and Kappa, computed from the confusion matrix, were used to assess the accuracy of irrigated cropland maps from 2010 to 2020 (Table 3). The assessment results indicate that the irrigated cropland maps generated using the random forest model exhibit high robustness. The OA consistently exceeds 0.85, and the Kappa coefficient is greater than 0.80. In addition, the UA and PA for irrigated cropland indicate that the maps produced in this study achieved satisfactory accuracy, with minimal misclassification and omission errors. The relatively low UA and PA for rain-fed cropland may be attributed to its fragmented nature. The 250 m spatial resolution is relatively coarse, leading to some misclassification. Overall, the classification results are sufficiently accurate for assessing the cooling effects of irrigated cropland.

Table 3. Accuracy of irrigated cropland and rain-fed cropland classification in 2010–2020.

Year	Irrigated Cropland		Rain-fed Cropland		OA	Kappa
	UA	PA	UA	PA		
2010	0.88	0.89	0.79	0.82	0.87	0.82
2012	0.90	0.89	0.85	0.84	0.88	0.85
2014	0.91	0.88	0.82	0.83	0.89	0.86
2016	0.86	0.92	0.81	0.77	0.88	0.84
2018	0.86	0.88	0.77	0.75	0.85	0.81
2020	0.87	0.84	0.82	0.85	0.87	0.84

To further validate the results, the irrigated cropland maps were compared with prefecture-level statistical data (<https://tj.nmg.gov.cn/datashow/pubmgr/publishmanage.htm>, accessed on 29 November 2024). The comparison showed satisfactory agreement between the maps and the statistical data, though the maps exhibited an overestimation. This is consistent with findings from previous studies on irrigated cropland mapping (Figure 7). The overestimation arises because the statistical data represent the effective irrigated area, whereas the maps capture the actual irrigated area, including marginal or partially irrigated zones [16]. Overall, the validation results confirm the reliability of the irrigated cropland maps, supporting their use in analyzing spatial and temporal changes in irrigated cropland and detecting associated cooling effects. These results demonstrate the robustness of the classification framework in capturing key patterns and dynamics in irrigated cropland.

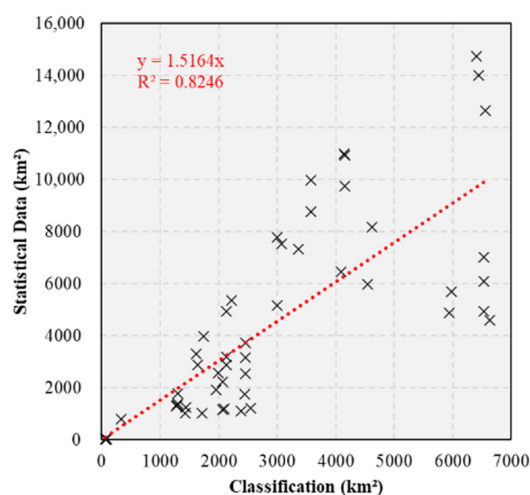


Figure 7. Validation of consistency between statistical data and classification results.

3.3. Spatial Distribution and Change in Irrigated Cropland

The spatial distribution of land use in Inner Mongolia in 2020 is shown in Figure 8. The spatial distribution of land use from west to east is roughly divided into bare land, grassland, and forest land, with scattered distribution of urban, cropland, and water bodies. Bare land and urban are the most widely distributed in the Inner Mongolia, with a total of 470,862.66 km². Bare land is primarily located in the western part of the study area, with scattered occurrences in the southeast. This is followed by grasslands with a total of 435,133.99 km², mainly in the central and southeastern part of the study area. Inner Mongolia has 208,768.12 km² of forest, mainly in the northeast.

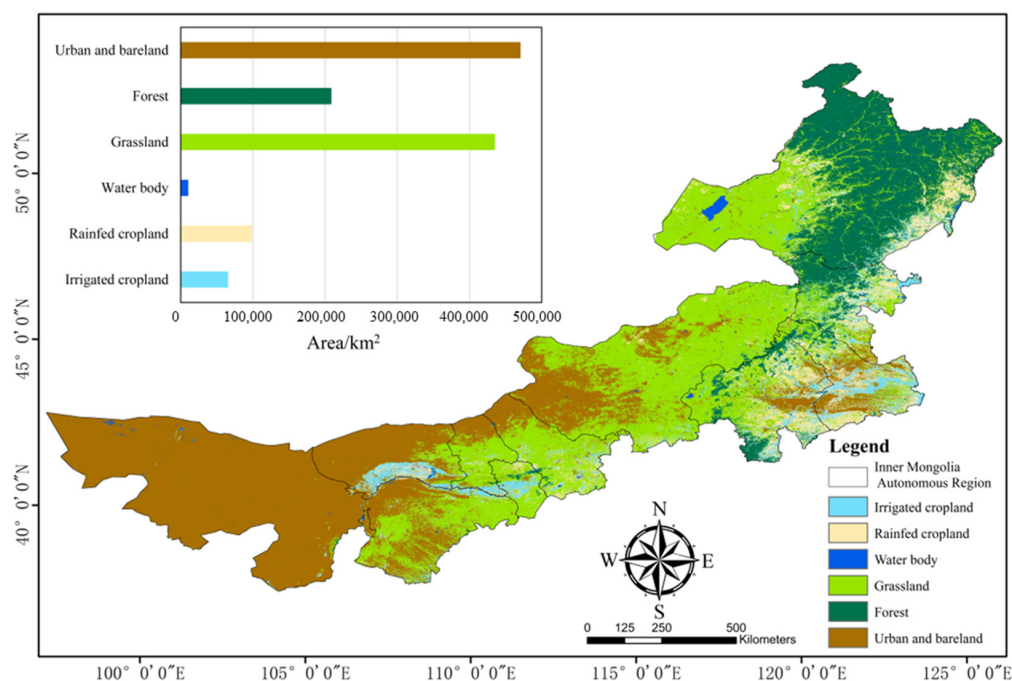


Figure 8. Classification results for land use in Inner Mongolia in 2020.

The cropland in Inner Mongolia is distributed in a strip-like mosaic among other land types, among which the area of irrigated cropland and rain-fed cropland are 87,317 km² and 138,392 km² respectively. In addition, irrigated cropland in Inner Mongolia is also scattered in low-lying areas of valleys. Rain-fed cropland is generally distributed in areas with poor irrigation conditions and large slopes around irrigated cropland, exhibiting a more fragmented and scattered distribution.

Analyzing the annual changes in irrigated cropland reveals a clear increasing trend in Inner Mongolia. Especially from 2014 to 2016, the area of irrigated cropland in Inner Mongolia expanded by 20,484.24 km² (Figure 9a,b). Between 2010 and 2014, the transfers into and out of irrigated cropland were roughly balanced. However the substantial increase in irrigated cropland between 2014 and 2016 was actually due to the transfer of large amounts of rain-fed cropland and non-cropland. Due to the long-term expansion of irrigated cropland, which has led to increased pressure on regional water resources, the increase in irrigated cropland was offset by a large amount of irrigated cropland being transferred out to rain-fed cropland between 2016 and 2020 (Figure 9b).

The 2020 and 2010 maps of irrigated cropland were analyzed to assess the spatial and temporal changes in irrigated cropland across the study area and to identify potential drivers behind these changes (Figure 10). From 2010 to 2020, irrigated cropland in Inner Mongolia generally increased, both in arid areas and in areas with a more intensive distribution of cropland, as well as in mountainous areas with more stringent land regulation (the Daxinganling Mountains in the northeast of the study area) [69]. In arid regions, this increase was more sporadic, mainly due to the reclamation and conversion of wasteland or

grassland into irrigated cropland (Figure 10c). In mountainous areas where land regulation is more stringent, especially under the constraint of China’s “return of cultivated land to forest” policy [70], the expansion of irrigated cropland was typically achieved by converting rain-fed cropland. However, there were many rounded fields in the same area in 2020, due to the Center-Pivot-Irrigation-Systems effect on rain-fed cropland, as evidenced by our mapping results (Figure 10a). In regions with relatively adequate water sources and better irrigation conditions, there is already a considerable amount of irrigated cropland. With the promotion of water-saving agriculture in Inner Mongolia, which makes it possible to irrigate more cropland with the same amount of freshwater resources, new water-saving irrigation facilities will be built (Figure 10b). Our observations also indicated a decline in irrigated cropland in certain areas, particularly in regions with a dense concentration of such land (Figure 10). This reduction may be attributed to fields being left fallow or to insufficient irrigation.

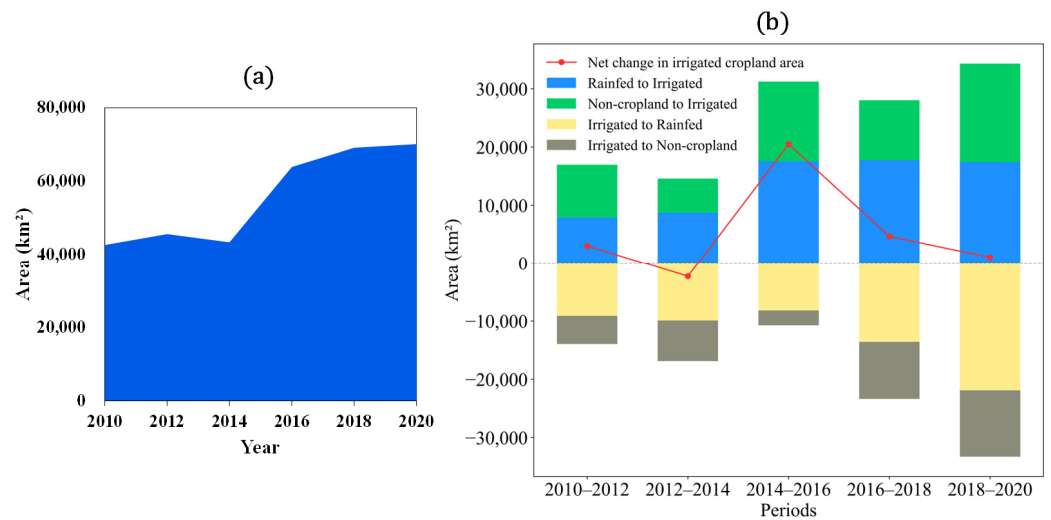


Figure 9. Changes in the area of irrigated cropland from 2010 to 2020. (a) Trends in irrigated cropland area. (b) Transfers in and out of irrigated cropland area and net changes in different periods.

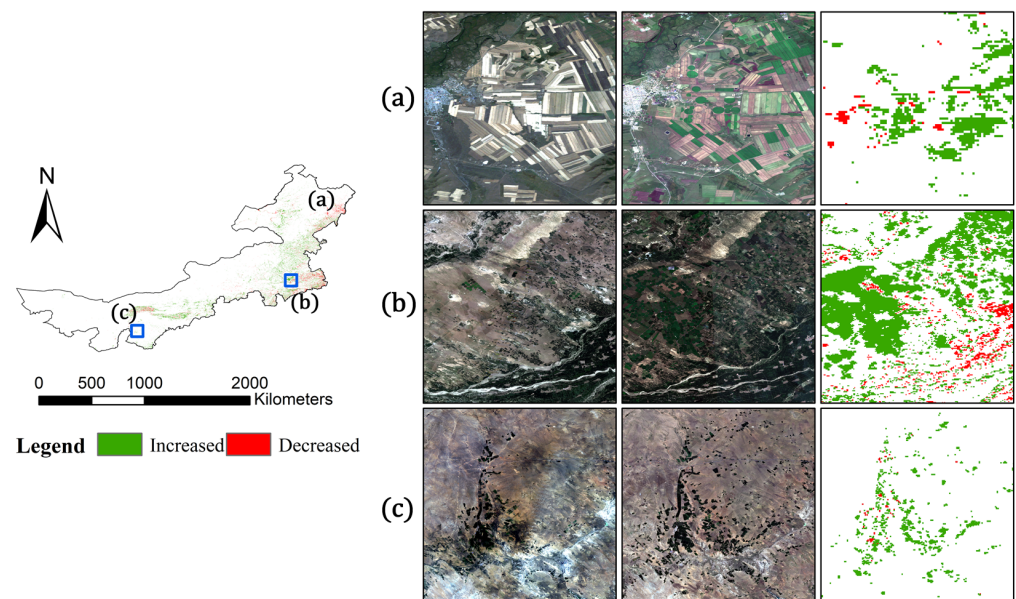


Figure 10. Changes in irrigated cropland in Inner Mongolia from 2010 to 2020. (a–c) Representative regions of three irrigated cropland expansions, with true-color images of Landsat-5 in 2010 and Sentinel-2 in 2020.

3.4. The Cooling Effect of Irrigated Cropland

Through quantitative analysis of the cooling effect of irrigated cropland in Inner Mongolia, we found that the LST of irrigated cropland was generally lower than that of rain-fed cropland, exhibiting diurnal, seasonal, and interannual differences. Based on multi-year data from 2010 to 2020, the average daily cooling effect of irrigation was $-0.25\text{ }^{\circ}\text{C}$. Most irrigated cropland (74.24%) experienced a cooling effect, while 25.76% of irrigated areas exhibited a warming effect (Figure 11a). The cooling effect of irrigated cropland peaked in July and August ($-0.64\text{ }^{\circ}\text{C}$), coinciding with the peak growing season when irrigation demand was highest due to elevated LST and increased evapotranspiration (Figure 11b). Outside of the growing season, the LST difference between irrigated and rain-fed cropland was significantly reduced, with a mean ΔLST of $-0.12\text{ }^{\circ}\text{C} \pm 0.03\text{ }^{\circ}\text{C}$ from October to April.

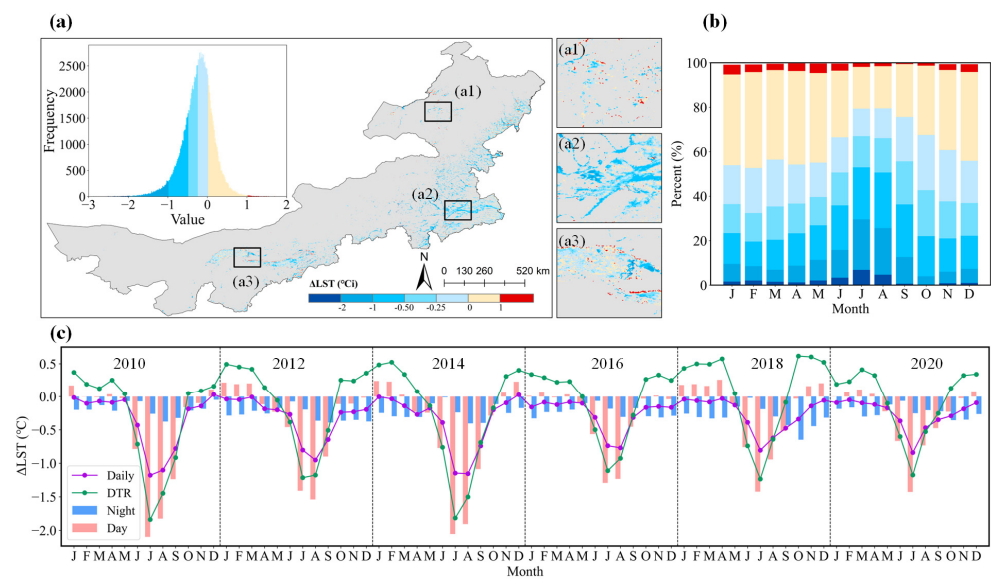


Figure 11. Detection results for irrigation cooling effects. (a) Maps, detailed maps, and frequency histograms of the multi-year average daily irrigation cooling. (a1–a3) Detailed maps of irrigation cooling effects in some regions. (b) Stacked frequency distribution of multi-year average daily irrigation cooling. (c) Interannual differences in cooling effects of irrigation for daytime LST, nighttime LST, daily mean LST, and DTR.

Diurnal differences were observed in the impact of irrigated cropland on LST (Figure 11c). Consistent with previous studies, our results show that irrigation has a stronger effect on daytime LST [14,71]. In winter, irrigated cropland shows a daytime warming effect, increasing the diurnal temperature range. In summer, the daytime cooling effect was much stronger than at night, resulting in a reduced diurnal temperature range. Notably, irrigation-induced reductions in nighttime LST were least pronounced during the early crop growth period (May to June). This may be due to heavy irrigation during this stage, where weaker daytime evapotranspiration results in soil water absorbing heat during the day and releasing it slowly at night [31].

Further experiments showed that the cooling effect of irrigation and evapotranspiration are strongly correlated. ΔET was calculated using the same moving window approach as that for ΔLST . Results indicate that ΔET and daily ΔLST exhibit highly correlated time-series trends. From June to September, when ΔET was highest, the irrigation cooling effect was also strongest (Figure 12a). Mapping the time-series trends onto a scatterplot revealed that irrigation-induced decreases in LST and increases in ET primarily occurred during summer and some autumn months. Additionally, ΔLST and ΔET exhibited a highly linear relationship, with an R^2 of 0.85 (Figure 12b). Higher LST leads to increased evapotranspiration, and irrigation further enhances evapotranspiration, thereby mitigating surface

temperature rise. These findings underscore the potential of irrigation to mitigate climate change risks.

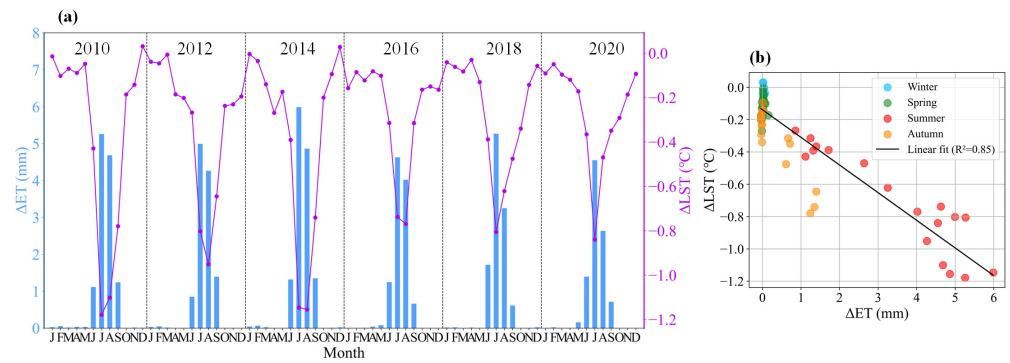


Figure 12. Multi-year trends in ΔET and daily ΔLST . (a) Time series trends in ΔET and daily ΔLST . (b) Consistency of ΔET and daily ΔLST .

Monthly correlation analysis between ΔLST and ΔET showed significant correlations for all months ($p < 0.05$). However, a strong negative correlation (Pearson correlation coefficient < -0.5) was observed only from June to September (Figure 13). For other months, while the correlation was weaker, the p -value remained significant due to the large sample size. These results highlight that the cooling effect of irrigation is most pronounced during the summer growing season, with evapotranspiration playing a key role in regulating LST during this period.

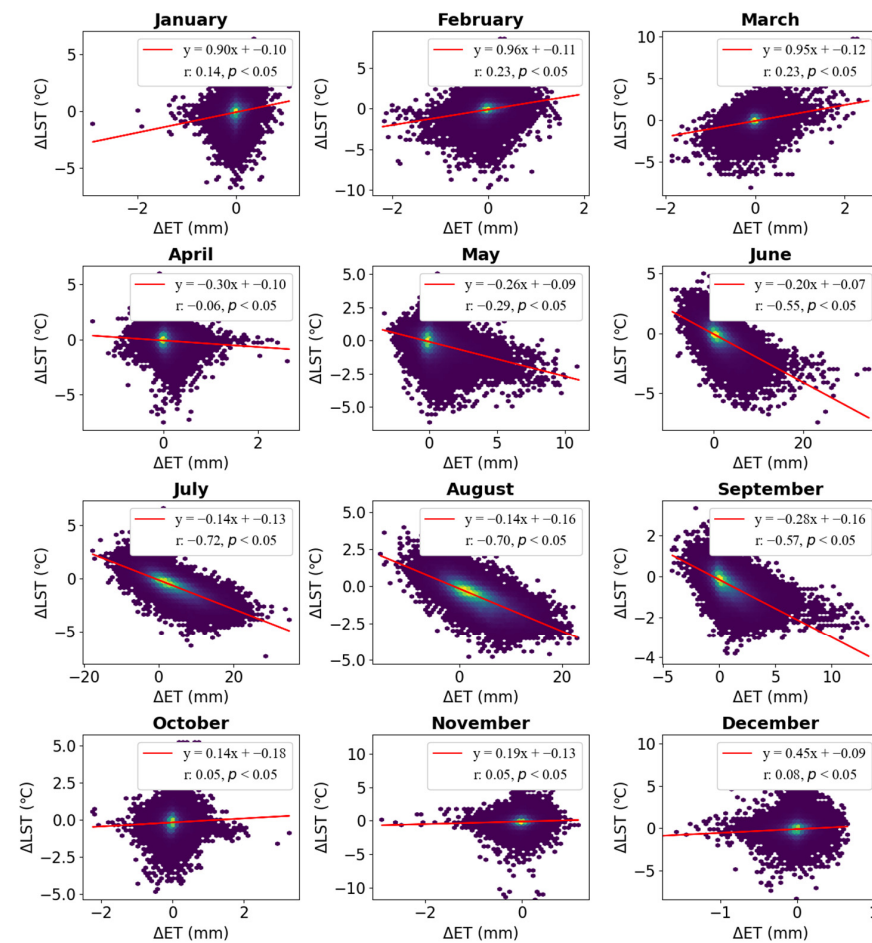


Figure 13. Monthly correlation and consistency of ΔET and daily ΔLST .

4. Discussion

4.1. Parameterization and Sensitivity Analysis for Quantification of Cooling Effects

The method used in this study to quantify the cooling effect of irrigated cropland relies on two main parameters, L and N . Sensitivity analyses were conducted to optimize parameter selection and evaluate the robustness of the method. Compared to N , the change in the window side length L had a greater impact on the quantitative results of the cooling effect, about $0.6\text{ }^{\circ}\text{C}$. An excessively large L can amplify the climatic difference between irrigated and rain-fed cropland, increasing the variance of the results, especially when L exceeds 35 km (Figure 14a). Conversely, an overly small L may cause the LST of rain-fed cropland pixels to be influenced by neighboring irrigated cropland pixels, resulting in an underestimation of the cooling effect [72]. To balance these factors, this study set L to 21 km , a value that minimized the decrease in ΔLST with increasing L while maintaining relatively low variance.

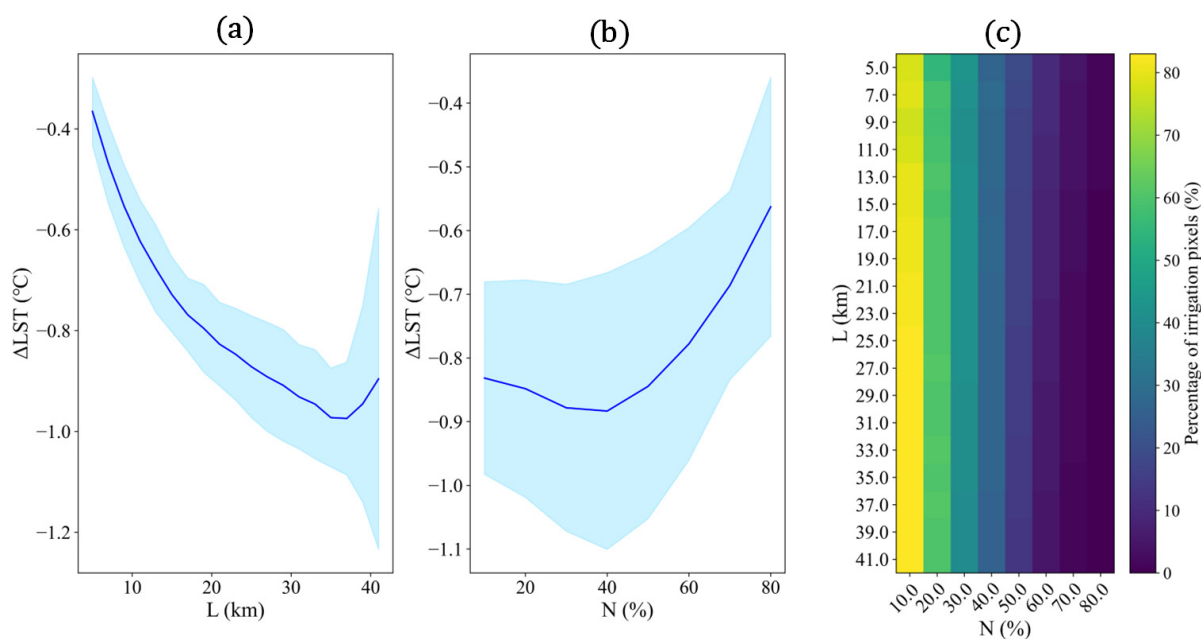


Figure 14. Sensitivity analysis for different combinations of L and N parameters. (a,b) Effects of different L and N parameters on the results of the quantification of the cooling effect. (c) Proportion of pixels of irrigated cropland detected under different combinations of parameters.

The proportion of rain-fed cropland pixels in the window, N , has relatively less effect on ΔLST (Figure 14b). Instead, N mainly affects the extent of irrigated cropland detection (Figure 14c). When N was set to 10%, the method ensured adequate detection of irrigated cropland while avoiding outliers. In practice, 10% of rain-fed cropland pixels within a 21 km window is sufficient to achieve reliable results without compromising the accuracy of the cooling effect assessment.

4.2. Causes and Possible Influences on the Cooling Effect of Irrigation

Irrigation exerts a cooling effect through its influence on different parts of the surface energy balance. It simultaneously increases soil evaporation, canopy retention, and vegetation transpiration [73], allowing more sensible heat fluxes to be redistributed as latent heat fluxes, thereby directly reducing LST [14,74]. Additionally, increased evapotranspiration can lead to enhanced cloud formation over the irrigated area, indirectly cooling the surface by reducing downward shortwave radiation [75]. In arid and semi-arid regions, irrigation ensures adequate water requirements for crops, resulting in denser canopies. These canopies absorb radiation for photosynthesis and have higher water content and specific heat capacity, leading to less warming compared to non-irrigated areas [76]. The additional

vegetative cover also enhances water uptake and transpiration in the root zone, further amplifying the cooling effect of irrigation [77]. This dynamic explains the strong correlation observed between ΔET and ΔLST , especially from June to September, when solar radiation is highest and vegetation is at its densest.

The effect of irrigation practices on the cooling effect is also significant, and it has been demonstrated that water-saving irrigation practices, such as drip irrigation, attenuate the cooling effect because water-saving irrigation drastically reduces the evaporation of soil moisture and canopy-trapped water evaporation by burying pipes and mulching [78]. Field experiments have also shown that water-saving irrigation techniques have lower Bowen ratios compared to conventional irrigation methods, which attenuates the cooling effect of irrigation [79]. Statistical data show that Inner Mongolia was also promoting water-saving irrigation technology between 2010 and 2020, increasing from 77% in 2010 to 92% in 2020 (Figure A3). Encouragingly, there was a correlation between the quantification of irrigation cooling effects in this study and changes in the proportion of water-saving irrigation in Inner Mongolia, with weaker irrigation cooling effects in years with a higher proportion of water-saving irrigation (Figure A3). This correlation may be influenced by other factors, and more in-depth studies are needed to isolate the effects of water-saving irrigation.

To validate the findings, the results of this study were compared with existing research (Table 4). Due to climatic differences in the study area and differences in methodology, there was large variation in the cooling effects of irrigated cropland, from $-0.096\text{ }^{\circ}\text{C}$ to $-5.1\text{ }^{\circ}\text{C}$, in different studies [14,31,71,80,81]. The cooling effects derived from this study are more conservative relative to those reported by Yang and Chen, likely because their methodologies overestimated cooling by treating natural vegetation as rain-fed cropland in semi-arid regions where rain-fed cropland is sparse [14,80]. Additionally, due to the large east–west span of Inner Mongolia, the climate in eastern Inner Mongolia is relatively wet, and the cooling effect of irrigated cropland in relatively wet regions is not as pronounced as in arid regions. Climatic conditions in Nebraska and Inner Mongolia are similar in that both are wetter in the east and have a greater distribution of irrigated cropland. The findings of this study are consistent with Li’s results in Nebraska [31], especially in July, which proves that the results of this study are relatively reliable.

Table 4. Quantification of the cooling effect of irrigation in different studies.

Index	Study Area	Parameter	Result	Reference
1	Nebraska (USA)	Daytime LST	$-1.63\text{ }^{\circ}\text{C}$ (July); $-1.19\text{ }^{\circ}\text{C}$ (August)	Li, et al., (2020) [31]
2	China	Daytime LST in arid regions	$-3.48 \pm 2.40\text{ }^{\circ}\text{C}$	Yang, et al., (2020) [14]
3	Northwest China	Daytime LST	$-0.28\text{ }^{\circ}\text{C}$ to $-0.69\text{ }^{\circ}\text{C}$	Zhang, et al., (2023) [71]
4	Globe	Daytime LST in arid regions	$-5.1\text{ }^{\circ}\text{C}$	Chen, et al., (2019) [80]
5	North China Plain	Daily LST	-0.098 K , -0.096 K and -0.165 K	Zhang, et al., (2022) [81]
6	Inner Mongolia, China	Daytime LST	$-0.36\text{ }^{\circ}\text{C}$; -1.61 (July)	This Study

4.3. Limitations and Prospects

The research framework proposed in this study is scalable and holds significant potential for remote sensing-based monitoring of regional irrigated cropland and analyzing the climatic effects of irrigation. However, it has two main shortcomings: the high labor and time costs associated with sample labeling, and the low spatial resolution of the irrigated cropland maps and LST data, which introduces uncertainty due to pixel mixing during cooling effect analysis.

The lack of publicly available datasets for irrigated cropland samples necessitates extensive manual labeling, resulting in substantial labor and time costs. Although Zhang et al. [11,82,83] proposed a sample generation method using statistical data, the collection process and inherent uncertainties in statistical data limit its applicability, particularly in regions with insufficient or unreliable data. Therefore, future research should focus on developing more efficient and reliable methods for generating irrigated cropland samples

to reduce manual effort and improve scalability, such as intersections from multiple-source existing maps, which could be a viable alternative.

The coarse spatial resolution of both the irrigated cropland maps and LST data further complicates the analysis [31], especially in regions with fragmented or sporadic farmland patches. Landsat data, with spectral bands ranging from the visible to the thermal infrared at a resolution of 30 to 60 m [84], may offer a promising alternative. Future research should prioritize leveraging Landsat data to reduce the impact of mixed pixels and improve the accuracy of irrigation cooling effect quantification.

5. Conclusions

This study presents an efficient framework for satellite monitoring of irrigated cropland dynamics and quantifying their associated cooling effects. By mapping irrigated cropland changes across Inner Mongolia from 2010 to 2020 using dense time-series vegetation indicators, our framework enables detailed tracking of agricultural expansion and its climatic impacts. The main conclusions of our study include the following: (1) The RF algorithm in the GEE platform outperforms the SVM algorithm in classifying irrigated cropland based on time-series NDVI and EVI, as evidenced by higher accuracy and more stable performance. (2) Irrigated cropland in Inner Mongolia increased significantly between 2010 and 2020, especially after 2014, when it increased the most. This expansion is primarily characterized by the conversion of desert grasslands or bare land into irrigated cropland in arid regions and the transformation of rain-fed cropland into irrigated cropland in forest-protected areas. (3) Irrigation reduced the daily LST by approximately 0.25 °C, with the most pronounced cooling effect of up to 0.64 °C observed during July and August, coinciding with peak evapotranspiration.

Collectively, the research framework proposed in this study has potential for monitoring irrigated cropland dynamics and assessing the impact of irrigation on climate. Meanwhile, this study provides a valuable tool for promoting climate-resilient agricultural practices. It represents a meaningful step toward sustainable agricultural adaptation under changing climate conditions.

Author Contributions: Conceptualization, L.L. and K.L.; methodology, L.L. and S.W.; validation, B.Y.; data curation, L.L.; writing—original draft preparation, L.L. and Y.B.; writing—review and editing, X.L.; visualization, L.L.; supervision, K.L.; project administration, K.L. and S.W.; funding acquisition, S.W. All authors have read and agreed to the published version of the manuscript.

Funding: This research was funded by the Key Program of Aerospace Information Innovation Institute of Chinese Academy of Sciences (grant number: E2Z211020F), the Inner Mongolia Autonomous Region Open Competition Projects (2023JBG50008), and the “Science for a Better Development of Inner Mongolia” Program (grant number: 2022EEDSKJXM003) of the Bureau of Science and Technology of the Inner Mongolia Autonomous Region.

Data Availability Statement: All of the data used in this study can be accessed and downloaded at Google Earth Engine (<https://earthengine.google.com/>, accessed on 29 November 2024). Maps of irrigated cropland with quantitative results of cooling effects are available by contacting the authors.

Acknowledgments: Thanks to Google Earth Engine for providing access to datasets and computational resources, which greatly facilitated this research; We also sincerely thank the anonymous reviewers for their helpful comments.

Conflicts of Interest: The authors declare no conflicts of interest.

Appendix A

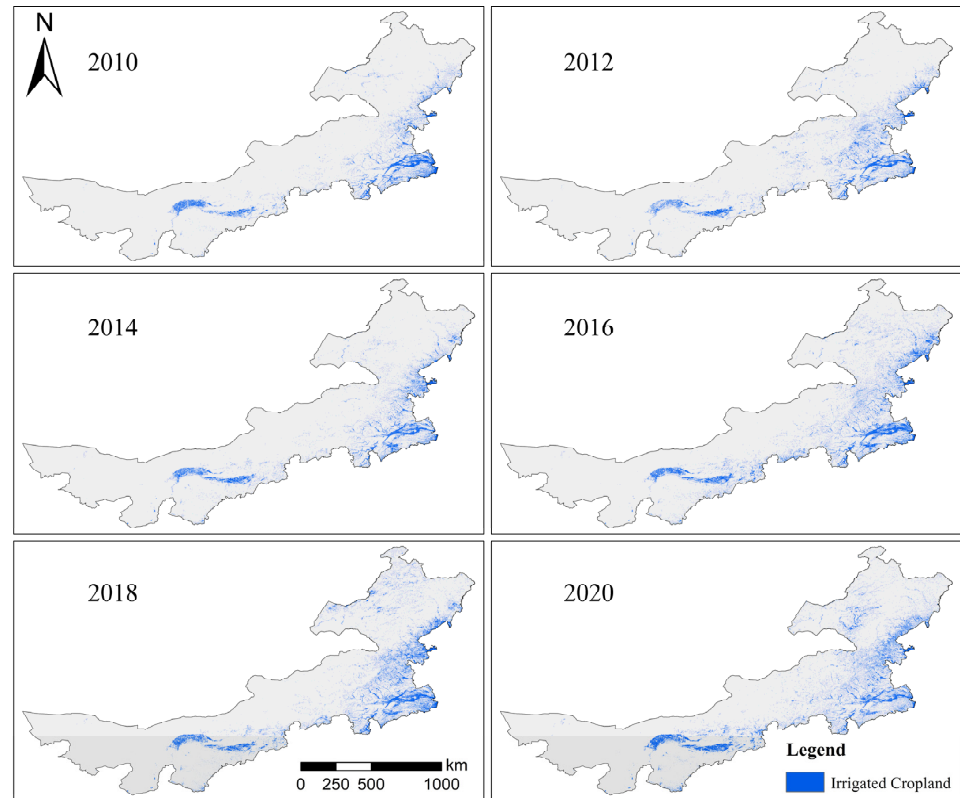


Figure A1. Map of irrigated cropland from 2010 to 2020.

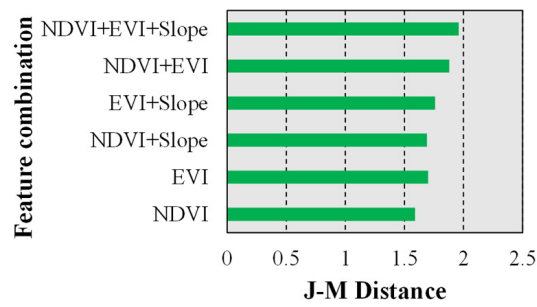


Figure A2. J-M distances for different combinations of features.

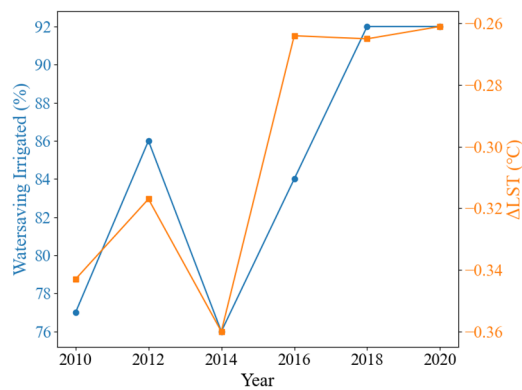


Figure A3. Changes in the proportion of water-saving irrigation and changes in the cooling effect of irrigation in Inner Mongolia from 2010 to 2020.

References

1. Gleick, P.H. Water in crisis: Paths to sustainable water use. *Ecol. Appl.* **1998**, *8*, 571–579. [CrossRef]
2. Cervantes, C.; Ozdogan, M.; Yang, Y.; Allez, G. Remote Sensing of Irrigated Agriculture: Opportunities and Challenges. *Remote Sens.* **2010**, *2*, 2274–2304. [CrossRef]
3. Viala, E. Water for food, water for life a comprehensive assessment of water management in agriculture. *Irrig. Drain. Syst.* **2008**, *22*, 127–129. [CrossRef]
4. Liu, K.; Li, X.; Long, X. Trends in groundwater changes driven by precipitation and anthropogenic activities on the southeast side of the Hu Line. *Environ. Res. Lett.* **2021**, *16*, 094032. [CrossRef]
5. Touge, Y.; Mbugua, J.M.; Kazama, S.; Khujanazarov, T.; Tanaka, K. Detecting Irrigation Effect on Surface Temperature using Modis and Land Surface Model in Whole Uzbekistan. In Proceedings of the IGARSS 2020—2020 IEEE International Geoscience and Remote Sensing Symposium, Waikoloa, HI, USA, 26 September–2 October 2020.
6. Zhou, D.; Xiao, J.; Froelking, S.; Liu, S.; Zhou, G. Croplands intensify regional and global warming according to satellite observations. *Remote Sens. Environ.* **2021**, *264*, 112585. [CrossRef]
7. Inner Mongolia Water Conservancy Department. Inner Mongolia Water Resources Bulletin. Available online: <http://slt.nmg.gov.cn/> (accessed on 1 June 2022).
8. Liu, K.; Li, X.; Wang, S.; Zhou, G. Past and future adverse response of terrestrial water storages to increased vegetation growth in drylands. *Npj Clim. Atmos. Sci.* **2023**, *6*, 113. [CrossRef]
9. Bo, Y.; Li, X.; Liu, K.; Wang, S.; Li, D.; Xu, Y.; Wang, M. Hybrid theory-guided data driven framework for calculating irrigation water use of three staple cereal crops in China. *Water Resour. Res.* **2024**, *60*, e2023WR035234. [CrossRef]
10. Ambika, A.K.; Wardlow, B.; Mishra, V. Remotely sensed high resolution irrigated area mapping in India for 2000 to 2015. *Sci. Data* **2016**, *3*, 160118. [CrossRef]
11. Zhang, C.; Dong, J.; Zuo, L.; Ge, Q. Tracking spatiotemporal dynamics of irrigated croplands in China from 2000 to 2019 through the synergy of remote sensing, statistics, and historical irrigation datasets. *Agric. Water Manag.* **2022**, *263*, 107458. [CrossRef]
12. Wu, B.; Tian, F.; Nabil, M.; Bofana, J.; Lu, Y.; Elnashar, A.; Beyene, A.N.; Zhang, M.; Zeng, H.; Zhu, W. Mapping global maximum irrigation extent at 30m resolution using the irrigation performances under drought stress. *Glob. Environ. Chang.* **2023**, *79*, 102652. [CrossRef]
13. Sacks, W.J.; Cook, B.I.; Buening, N.; Levis, S.; Helkowski, J.H. Effects of global irrigation on the near-surface climate. *Clim. Dyn.* **2009**, *33*, 159–175. [CrossRef]
14. Yang, Q.; Huang, X.; Tang, Q. Irrigation cooling effect on land surface temperature across China based on satellite observations. *Sci. Total Environ.* **2020**, *705*, 135984. [CrossRef]
15. Liu, G.; Wang, W. Irrigation-induced crop growth enhances irrigation cooling effect over the north China plain by increasing transpiration. *Water Resour. Res.* **2023**, *59*, e2022WR034142. [CrossRef]
16. Tan, M.; Ran, Y.; Feng, M.; Dong, G.; Du, D.; Zhu, G.; Nian, Y.; Li, X. Long-term monitoring of the annual irrigated cropland extent in fragmented and heterogeneous arid landscapes using machine learning and Landsat imagery. *Water Resour. Res.* **2024**, *60*, e2023WR036945. [CrossRef]
17. Salmon, J.M.; Friedl, M.A.; Froelking, S.; Wisser, D.; Douglas, E.M. Global rain-fed, irrigated, and paddy croplands: A new high resolution map derived from remote sensing, crop inventories and climate data. *Int. J. Appl. Earth Obs. Geoinf.* **2015**, *38*, 321–334. [CrossRef]
18. Xie, Y.; Lark, T.J. Mapping annual irrigation from Landsat imagery and environmental variables across the conterminous United States. *Remote Sens. Environ.* **2021**, *260*, 112445. [CrossRef]
19. Pervez, M.S.; Brown, J.F. Mapping irrigated lands at 250-m scale by merging MODIS data and national agricultural statistics. *Remote Sens.* **2010**, *2*, 2388–2412. [CrossRef]
20. Yao, Z.; Cui, Y.; Geng, X.; Chen, X.; Li, S. Mapping irrigated area at field scale based on the optical TRapezoid Model (OPTRAM) using landsat images and google earth engine. *Trans. Geosci. Remote Sens.* **2022**, *60*, 1–11. [CrossRef]
21. Dari, J.; Quintana-Seguí, P.; Escorihuela, M.J.; Stefan, V.; Brocca, L.; Morbidelli, R. Detecting and mapping irrigated areas in a Mediterranean environment by using remote sensing soil moisture and a land surface model. *J. Hydrol.* **2021**, *596*, 126129. [CrossRef]
22. Lawston, P.M.; Santanello, J.A., Jr.; Kumar, S.V. Irrigation signals detected from SMAP soil moisture retrievals. *Geophys. Res. Lett.* **2017**, *44*, 11–860. [CrossRef]
23. Mehta, P.; Siebert, S.; Kummu, M.; Deng, Q.; Ali, T.; Marston, L.; Xie, W.; Davis, K.F. Half of twenty-first century global irrigation expansion has been in water-stressed regions. *Nat. Water* **2024**, *2*, 254–261. [CrossRef]
24. Zohaib, M.; Choi, M. Satellite-based global-scale irrigation water use and its contemporary trends. *Sci. Total Environ.* **2020**, *714*, 136719. [CrossRef]
25. Ahmad, J.A.; Forman, B.A.; Getirana, A.; Kumar, S.V. Influence of SMAP soil moisture retrieval assimilation on runoff estimation across South Asia. *J. Hydrol.* **2024**, *639*, 131550. [CrossRef]
26. Zhang, X.; Liu, K.; Wang, S.; Long, X.; Li, X. A rapid model (COV_PSDI) for winter wheat mapping in fallow rotation area using MODIS NDVI time-series satellite observations: The case of the Heilonggang region. *Remote Sens.* **2021**, *13*, 4870. [CrossRef]
27. Xiang, K.; Ma, M.; Liu, W.; Dong, J.; Zhu, X.; Yuan, W. Mapping irrigated areas of northeast China in comparison to natural vegetation. *Remote Sens.* **2019**, *11*, 825. [CrossRef]

28. Zhang, C.; Dong, J.; Ge, Q. Irrimap_CN: Annual irrigation maps across China in 2000–2019 based on satellite observations, environmental variables, and machine learning. *Remote Sens. Environ.* **2022**, *280*, 113184. [CrossRef]
29. Li, X.; Wu, T.; Liu, K.; Li, Y.; Zhang, L. Evaluation of the Chinese fine spatial resolution hyperspectral satellite TianGong-1 in urban land-cover classification. *Remote Sens.* **2016**, *8*, 438. [CrossRef]
30. Troy, T.J.; Kipgen, C.; Pal, I. The impact of climate extremes and irrigation on US crop yields. *Environ. Res. Lett.* **2015**, *10*, 054013. [CrossRef]
31. Li, Y.; Guan, K.; Peng, B.; Franz, T.E.; Wardlow, B.; Pan, M. Quantifying irrigation cooling benefits to maize yield in the US Midwest. *Glob. Chang. Biol.* **2020**, *26*, 3065–3078. [CrossRef]
32. Gao, K.; Santamouris, M.; Feng, J. On the cooling potential of irrigation to mitigate urban heat island. *Sci. Total Environ.* **2020**, *740*, 139754. [CrossRef] [PubMed]
33. Liu, J.; Jin, J.; Niu, G.Y. Effects of irrigation on seasonal and annual temperature and precipitation over China simulated by the WRF model. *J. Geophys. Res. Atmos.* **2021**, *126*, e2020JD034222. [CrossRef]
34. Liu, G.; Wang, W.; Shao, Q.; Wei, J.; Zheng, J.; Liu, B.; Chen, Z. Simulating the climatic effects of irrigation over China by using the WRF-Noah model system with mosaic approach. *J. Geophys. Res. Atmos.* **2021**, *126*, e2020JD034428. [CrossRef]
35. Kioutsioukis, I.; de Meij, A.; Jakobs, H.; Katragkou, E.; Vinuesa, J.-F.; Kazantzidis, A. High resolution WRF ensemble forecasting for irrigation: Multi-variable evaluation. *Atmos. Res.* **2016**, *167*, 156–174. [CrossRef]
36. Hu, Q.; Pan, F.; Pan, X.; Zhang, D.; Li, Q.; Pan, Z.; Wei, Y. Spatial analysis of climate change in Inner Mongolia during 1961–2012, China. *Appl. Geogr.* **2015**, *60*, 254–260. [CrossRef]
37. Li, C.; Wang, J.; Hu, R.; Yin, S.; Bao, Y.; Ayal, D.Y. Relationship between vegetation change and extreme climate indices on the Inner Mongolia Plateau, China, from 1982 to 2013. *Ecol. Indic.* **2018**, *89*, 101–109. [CrossRef]
38. United States Geological Survey Description of MOD13Q1 v006 Product. Available online: <https://lpdaac.usgs.gov/products/mod13q1v006/> (accessed on 28 June 2022).
39. Tucker, C.J. Red and photographic infrared linear combinations for monitoring vegetation. *Remote Sens. Environ.* **1979**, *8*, 127–150. [CrossRef]
40. Zeng, H.; Bingfang, W.U.; Zou, W.; Yan, N.; Zhang, M. Performance comparison of crop condition assessments in irrigated and rain-fed areas: A case study in Nebraska. *J. Remote Sens.* **2015**, *19*, 560–567.
41. Corgne, S. Identifying Seasonal Groundwater-Irrigated Cropland Using Multi-Source NDVI Time-Series Images. *Remote Sens.* **2021**, *13*, 1960. [CrossRef]
42. Gumma, M.K.; Thenkabail, P.S.; Teluguntla, P.; Whitbread, A.M. Chapter 9-Indo-Ganges River Basin Land Use/Land Cover (LULC) and Irrigated Area Mapping. In *Indus River Basin*; Khan, S.I., Adams, T.E., Eds.; Elsevier: Amsterdam, The Netherlands, 2019; pp. 203–228.
43. Huang, S.; Tang, L.; Hupy, J.P.; Wang, Y.; Shao, G. A commentary review on the use of normalized difference vegetation index (NDVI) in the era of popular remote sensing. *J. For. Res.* **2020**, *32*, 1–6. [CrossRef]
44. Huete, A.; Didan, K.; Miura, T.; Rodriguez, E.P.; Gao, X.; Ferreira, L.G. Overview of the radiometric and biophysical performance of the MODIS vegetation indices. *Remote Sens. Environ.* **2002**, *83*, 195–213. [CrossRef]
45. Chen, J.; Jönsson, P.; Tamura, M.; Gu, Z.; Matsushita, B.; Eklundh, L. A simple method for reconstructing a high-quality NDVI time-series data set based on the Savitzky–Golay filter. *Remote Sens. Environ.* **2004**, *91*, 332–344. [CrossRef]
46. Cao, R.; Chen, Y.; Shen, M.; Chen, J.; Zhou, J.; Wang, C.; Yang, W. A simple method to improve the quality of NDVI time-series data by integrating spatiotemporal information with the Savitzky–Golay filter. *Remote Sens. Environ.* **2018**, *217*, 244–257. [CrossRef]
47. de Andrade, M.D.; Delgado, R.C.; da Costa de Menezes, S.J.M.; de Ávila Rodrigues, R.; Teodoro, P.E.; da Silva Junior, C.A.; Pereira, M.G. Evaluation of the MOD11A2 product for canopy temperature monitoring in the Brazilian Atlantic Forest. *Environ. Monit. Assess.* **2021**, *193*, 45. [CrossRef] [PubMed]
48. Du, J.; Jacinthe, P.A.; Zhou, H.; Xiang, X.; Zhao, B.; Wang, M.; Song, K. Monitoring of water surface temperature of Eurasian large lakes using MODIS land surface temperature product. *Hydrol. Process.* **2020**, *34*, 3582–3595. [CrossRef]
49. Mu, Q.; Zhao, M.; Running, S.W. MODIS global terrestrial evapotranspiration (ET) product (NASA MOD16A2/A3). *Algorithm Theor. Basis Doc. Collect.* **2013**, *5*, 381–394.
50. Farr, T.G.; Rosen, P.A.; Caro, E.; Crippen, R.; Duren, R.; Hensley, S.; Kobrick, M.; Paller, M.; Rodriguez, E.; Roth, L. The Shuttle Radar Topography Mission. *Rev. Geophys.* **2007**, *45*, 361. [CrossRef]
51. Sharma, A.K.; Hubert-Moy, L.; Buvaneshwari, S.; Sekhar, M.; Ruiz, L.; Bandyopadhyay, S.; Corgne, S. Irrigation History Estimation Using Multitemporal Landsat Satellite Images: Application to an Intensive Groundwater Irrigated Agricultural Watershed in India. *Remote Sens.* **2018**, *10*, 893. [CrossRef]
52. Brown, J.F.; Pervez, M.S. Merging remote sensing data and national agricultural statistics to model change in irrigated agriculture. *Agric. Syst.* **2014**, *127*, 28–40. [CrossRef]
53. Sen, R.; Goswami, S.; Chakraborty, B. Jeffries–Matusita distance as a tool for feature selection. In Proceedings of the 2019 International Conference on Data Science and Engineering (ICDSE), Patna, India, 26–28 September 2019; pp. 15–20.
54. Li, L.; Solana, C.; Canters, F.; Kervyn, M. Testing random forest classification for identifying lava flows and mapping age groups on a single Landsat 8 image. *J. Volcanol. Geotherm. Res.* **2017**, *345*, 109–124. [CrossRef]

55. Msofe, N.K.; Sheng, L.; Li, Z.; Lyimo, J. Impact of Land Use/Cover Change on Ecosystem Service Values in the Kilombero Valley Floodplain, Southeastern Tanzania. *Forests* **2020**, *11*, 109. [CrossRef]
56. Ge, G.; Shi, Z.; Zhu, Y.; Yang, X.; Hao, Y. Land use/cover classification in an arid desert-oasis mosaic landscape of China using remote sensed imagery: Performance assessment of four machine learning algorithms. *Glob. Ecol. Conserv.* **2020**, *22*, e00971. [CrossRef]
57. Lin, Y.; Yu, J.; Ying, M.; Shen, M. A Study on monitoring Land Use/Cover Change of mining area based on Ticket-Voting SVM classification. In Proceedings of the 19th National Symposium on Remote Sensing of China—Remote Sensing of the Environment, Xi'an, China, 20–23 September 2014. [CrossRef]
58. Serban, R.-D.; Serban, M.; He, R.; Jin, H.; Li, Y.; Li, X.; Wang, X.; Li, G. 46-Year (1973-2019) Permafrost Landscape Changes in the Hola Basin, Northeast China Using Machine Learning and Object-Oriented Classification. *Remote Sens.* **2021**, *13*, 1910. [CrossRef]
59. Ul Din, S.; Mak, H.W.L. Retrieval of Land-Use/Land Cover Change (LUCC) Maps and Urban Expansion Dynamics of Hyderabad, Pakistan via Landsat Datasets and Support Vector Machine Framework. *Remote Sens.* **2021**, *13*, 3337. [CrossRef]
60. Breiman, L. Random forests. *Mach. Learn.* **2001**, *45*, 5–32. [CrossRef]
61. Google Earth Engine. Reference of ee.Classifier.smileRandomForest. Available online: <https://developers.google.com/earth-engine/apidocs/ee-classifier-smilerandomforest> (accessed on 1 June 2022).
62. Li, X.; Li, L.; Chen, L.; Zhang, T.; Xiao, J.; Chen, L. Random Forest Estimation and Trend Analysis of PM2.5 Concentration over the Huaihai Economic Zone, China (2000–2020). *Sustainability* **2022**, *14*, 8520. [CrossRef]
63. Cortes, C.; Vapnik, V. Support-vector networks. *Mach. Learn.* **1995**, *20*, 273–297. [CrossRef]
64. Duro, D.C.; Franklin, S.E.; Dube, M.G. A comparison of pixel-based and object-based image analysis with selected machine learning algorithms for the classification of agricultural landscapes using SPOT-5 HRG imagery. *Remote Sens. Environ.* **2012**, *118*, 259–272. [CrossRef]
65. Google Earth Engine. Reference of ee.Classifier.libsvm. Available online: <https://developers.google.com/earth-engine/apidocs/ee-classifier-libsvm> (accessed on 1 June 2022).
66. Teluguntla, P.; Thenkabail, P.S.; Oliphant, A.; Xiong, J.; Gumma, M.K.; Congalton, R.G.; Yadav, K.; Huete, A. A 30-m landsat-derived cropland extent product of Australia and China using random forest machine learning algorithm on Google Earth Engine cloud computing platform. *ISPRS J. Photogramm. Remote Sens.* **2018**, *144*, 325–340. [CrossRef]
67. Gumma, M.K.; Thenkabail, P.S.; Teluguntla, P.G.; Oliphant, A.; Xiong, J.; Giri, C.; Pyla, V.; Dixit, S.; Whitbread, A.M. Agricultural cropland extent and areas of South Asia derived using Landsat satellite 30-m time-series big-data using random forest machine learning algorithms on the Google Earth Engine cloud. *GISci. Remote Sens.* **2020**, *57*, 302–322. [CrossRef]
68. Shetty, S.; Gupta, P.K.; Belgiu, M.; Srivastav, S. Assessing the effect of training sampling design on the performance of machine learning classifiers for land cover mapping using multi-temporal remote sensing data and google earth engine. *Remote Sens.* **2021**, *13*, 1433. [CrossRef]
69. Chen, K.; Wang, J.; He, Y.; Zhang, L. Estimations of forest carbon storage and carbon sequestration potential of key state-owned forest region in Daxing'anling, Heilongjiang province. *Ecol. Environ.* **2022**, *31*, 1725.
70. Liu, W.; Qi, Y.; Jiang, Q.o.; Nie, C. Quantitative simulation of dynamic changes in cultivated land in areas of reclamation and returning cultivated land to forest or pastures under RCPs climate scenarios. *Agric. Sci. Technol.* **2016**, *17*, 178.
71. Zhang, C.; Ge, Q.; Dong, J.; Zhang, X.; Li, Y.; Han, S. Characterizing spatial, diurnal, and seasonal patterns of agricultural irrigation expansion-induced cooling in Northwest China from 2000 to 2020. *Agric. For. Meteorol.* **2023**, *330*, 109304. [CrossRef]
72. Faroqi, H. Analyzing effects of environmental indices on satellite remote sensing land surface temperature using spatial regression models. *Appl. Geomat.* **2024**, *16*, 629–638. [CrossRef]
73. Zheng, C.; Jia, L.; Hu, G. Global land surface evapotranspiration monitoring by ETMonitor model driven by multi-source satellite earth observations. *J. Hydrol.* **2022**, *613*, 128444. [CrossRef]
74. Lobell, D.B.; Bonfils, C.J.; Kueppers, L.M.; Snyder, M.A. Irrigation cooling effect on temperature and heat index extremes. *Geophys. Res. Lett.* **2008**, *35*, L09705. [CrossRef]
75. Garcia-Carreras, L.; Marsham, J.H.; Spracklen, D.V. Observations of increased cloud cover over irrigated agriculture in an arid environment. *J. Hydrometeorol.* **2017**, *18*, 2161–2172. [CrossRef]
76. Lin, J.; Zhou, L.; Wu, J.; Han, X.; Zhao, B.; Chen, M.; Liu, L. Water stress significantly affects the diurnal variation of solar-induced chlorophyll fluorescence (SIF): A case study for winter wheat. *Sci. Total Environ.* **2024**, *908*, 168256. [CrossRef] [PubMed]
77. Feldman, A.F.; Short Gianotti, D.J.; Dong, J.; Trigo, I.F.; Salvucci, G.D.; Entekhabi, D. Tropical surface temperature response to vegetation cover changes and the role of drylands. *Glob. Chang. Biol.* **2023**, *29*, 110–125. [CrossRef] [PubMed]
78. Zhang, C.; Dong, J.; Leng, G.; Doughty, R.; Zhang, K.; Han, S.; Zhang, G.; Zhang, X.; Ge, Q. Attenuated cooling effects with increasing water-saving irrigation: Satellite evidence from Xinjiang, China. *Agric. For. Meteorol.* **2023**, *333*, 109397. [CrossRef]
79. Fu, J.; Kang, S.; Zhang, L.; Li, X.; Gentile, P.; Niu, J. Amplified warming induced by large-scale application of water-saving techniques. *Environ. Res. Lett.* **2022**, *17*, 034018. [CrossRef]
80. Chen, L.; Dirmeyer, P.A. Global observed and modelled impacts of irrigation on surface temperature. *Int. J. Climatol.* **2019**, *39*, 2587–2600. [CrossRef]
81. Zhang, Z.; Lin, A.; Zhao, L.; Zhao, B. Attribution of local land surface temperature variations response to irrigation over the North China Plain. *Sci. Total Environ.* **2022**, *826*, 154104. [CrossRef]

82. Zhang, C.; Dong, J.; Xie, Y.; Zhang, X.; Ge, Q. Mapping irrigated croplands in China using a synergetic training sample generating method, machine learning classifier, and Google Earth Engine. *Int. J. Appl. Earth Obs. Geoinf.* **2022**, *112*, 102888. [[CrossRef](#)]
83. Zhang, C.; Dong, J.; Ge, Q. Mapping 20 years of irrigated croplands in China using MODIS and statistics and existing irrigation products. *Sci. Data* **2022**, *9*, 407. [[CrossRef](#)] [[PubMed](#)]
84. Wulder, M.A.; Roy, D.P.; Radeloff, V.C.; Loveland, T.R.; Anderson, M.C.; Johnson, D.M.; Healey, S.; Zhu, Z.; Scambos, T.A.; Pahlevan, N. Fifty years of Landsat science and impacts. *Remote Sens. Environ.* **2022**, *280*, 113195. [[CrossRef](#)]

Disclaimer/Publisher's Note: The statements, opinions and data contained in all publications are solely those of the individual author(s) and contributor(s) and not of MDPI and/or the editor(s). MDPI and/or the editor(s) disclaim responsibility for any injury to people or property resulting from any ideas, methods, instructions or products referred to in the content.